CRYSTAL GROWTH & DESIGN

pubs.acs.org/crystal

Article

Phosphorus···Iodine Halogen Bonding in Cocrystals of Bis(diphenylphosphino)ethane (dppe) and *p*-Diiodotetrafluorobenzene (*p*-F_4DIB)

Adam M. Siegfried, Hadi D. Arman, Khadijatul Kobra, Kunhuan Liu, Andrew J. Peloquin, Colin D. McMillen, Timothy Hanks, and William T. Pennington*

Cite This: *Cryst. Growth Des.* 2020, 20, 7460–7469

Read Online

ACCESS | Metrics & More | Article Recommendations | Supporting Information

ABSTRACT: Three new cocrystals of bis(diphenylphosphino)ethane (dppe) and *p*-diiodotetrafluorobenzene (*p*-F_4DIB) were studied using single-crystal X-ray crystallography. Two polymorphs containing a 1:1 dppe:*p*-F_4DIB ratio were obtained, each displaying strong P···I halogen bonding along steplike chains. Additionally, a cocrystal with a 1:3 dppe:*p*-F_4DIB ratio was studied. This cocrystal displays a similar main steplike chain to the 1:1 cocrystals, with pendant *p*-F_4DIB molecules along the chain. In all three of the cocrystals, face-to-face and face-to-edge interactions involving both the phenyl rings and the perfluorobenzene rings contribute to the packing of the halogen bonded chains. Computational studies, including Hirshfeld surface analysis and ab initio calculations, were conducted to further elucidate the varying factors contributing to the packing of the cocrystals and the resulting structural stability.

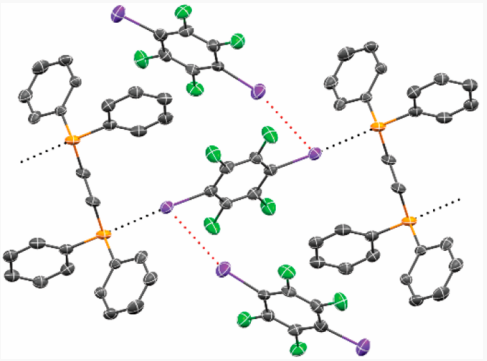

1. INTRODUCTION

Halogen bonding (X-bonding, X = Cl, Br, I) has been defined by the IUPAC as "a net attractive interaction between an electrophilic region associated with a halogen atom in a molecular entity and a nucleophilic region in another, or the same, molecular entity."[1] The emerging utility of this interaction is evident in a wide variety of fields, such as supramolecular chemistry,[2] anion detection,[3] biological systems,[4] and many other applications.[5,6] These have recently been exhaustively reviewed in an excellent contribution from Resnati and the Milano group.[7]

Our studies of halogen bonding have focused on cataloging supramolecular synthons involving a wide variety of halogen bonding acceptors, including nitrogen,[8−14] sulfur,[15,16] selenium,[17] iodide,[18] and more recently triiodide anions.[19] Phosphorus should also be a good candidate as a halogen-bonding acceptor due to the softness of the phosphorus atom.[20] Despite this, phosphorus acceptors with organohalogens are rare, with only 13 examples found in a CSD[21] search for P···X-C contacts.[22] Those involving chlorine, bromine, and iodine fit within expected geometric parameters for P···I for halogen bonding, while those involving fluorine exhibit greater deviations, as expected.[23,24] Expanding the scope of compounds having P···X-C contacts may be useful in establishing crystal engineering principles based on these rare halogen bonding interactions.

Here, we report the preparation and structural characterization of halogen bonded cocrystals of the organoiodine, 2,3,5,6-tetrafluoro-1,4-diodobenzene (*p*-F_4DIB), with the phosphorus halogen bond acceptor, bis(diphenylphosphino)-ethane (dppe), including two polymorphs with a 1:1 stoichiometry (X-acceptor:X-donor) and one form of a 1:3 stoichiometry. Diphosphines, like dppe, have been extensively employed in coordination chemistry as both bidentate ligands and bridging ligands but have not been utilized as a halogen bond acceptor to date. Crystals were grown by slow evaporation of solvent, and microcrystalline powders could be prepared by mechanochemical techniques.[25] In addition to I···P halogen bonding, the phenyl rings of dppe form a variety of phenyl embraces[26] involving edge-to-face (*ef*), vertex-to-face (*vf*), and offset face-to-face (*ff*) interactions that extend the structures into three dimensions. The contribution of these interactions play an important role in stabilizing crystal structures, providing a reliable secondary structural synthon for crystal design.

2. EXPERIMENTAL SECTION

2.1. Materials. 2,3,5,6-Tetrafluoro-1,4-diodobenzene (*p*-F_4DIB) ($C_6F_4I_2$, 98%, CAS registry no. 392-57-4) was purchased from Matrix

Received: August 12, 2020
Revised: September 21, 2020
Published: September 22, 2020

https://dx.doi.org/10.1021/acs.cgd.0c01129
Cryst. Growth Des. 2020, 20, 7460–7469

Scientific, SC, USA. Bis(diphenylphosphino)ethane (dppe) ($C_{26}H_{24}P_2$, 99%, CAS registry no. 1663-45-2) was purchased from Sigma-Aldrich. Chloroform ($CHCl_3$, 99%, CAS registry no. 67-66-3) and pentane (C_5H_{12}, 95%, CAS registry no. 109-66-0) from Fisher Chemical were the solvents used in the syntheses. All chemicals were used as received without further purification.

2.2. Synthesis of dppe·*p*-F_4DIB Polymorphs. Colorless, single crystals of dppe·*p*-F_4DIB were grown using 4 mg (0.01 mmol) of dppe and 4 mg (0.01 mmol) of *p*-F_4DIB dissolved in pentane or chloroform with slow evaporation. Chloroform produced the monoclinic polymorph, and pentane produced the triclinic polymorph. Elemental analysis was performed with a PerkinElmer 2400 SeriesII CHNS/O elemental analyzer, $\%_{exp}$ ($\%_{calc}$): %C 47.43 (48.03); %H 3.02 (2.96). A completely pure sample of the triclinic form could only be made by mechanochemistry, and elemental analysis was not deemed necessary.

2.3. Synthesis of dppe·3(*p*-F_4DIB). Colorless, single crystals of dppe·3(*p*-F_4DIB) were grown using 4 mg (0.01 mmol) of dppe and 12 mg (0.03 mmol) of *p*-F_4DIB dissolved in pentane with slow evaporation. Elemental analysis was performed with a PerkinElmer 2400 SeriesII CHNS/O elemental analyzer, $\%_{exp}$ ($\%_{calc}$): %C 33.02 (32.95); %H 1.54 (1.51).

2.4. Mechanosynthesis. Mechanosynthesis was carried out using a Wig-L-Bug ball mill with a 1 min timer. Appropriate molar ratios were loaded into a steel vial (0.1 g total mass minimum) with a steel ball bearing and ground from 15 s to 20 min. Powder was then removed from the steel vial for XRD, DSC/TGA, and melting point analyses.

2.5. Thermal Analysis. Simultaneous differential scanning calorimetry (DSC) and thermal gravimetric analysis (TGA) measurements were carried out in air using a TA Instruments SDT Q600. Sample masses ranged from 2 to 10 mg. Samples were heated from 20 to 300 °C at a rate of 2 °C/min. Melting points were also measured using an SRS DigiMelt MPA160 melting point apparatus.

2.6. X-ray Diffraction. Single-crystal X-ray intensity data were collected at 153 ± 1 K using a Rigaku AFC8S diffractometer equipped with a graphite monochromator and Mo Kα radiation (λ = 0.71073 Å), coupled with a Mercury CCD detector. Data were collected using ω scans of 0.5° with an X-ray exposure of 20−30 s depending on the diffraction quality of the crystal. Crystalclear software by Molecular Structure Corporation (MSC) was used for the instrument control, integration, and scaling. The structures were solved by direct methods (SHELXS) and refined by full matrix least-squares (SHELXL) techniques on F^2.[27] All non-hydrogen atoms were refined anisotropically, and hydrogen atoms attached to carbon atoms were placed in calculated positions using riding models. Crystallographic data are reported in Table 1, and the structures are deposited with the CCDC, deposition numbers 2021949−2021951. Powder X-ray diffraction measurements were made using a Rigaku Ultima IV diffractometer with Cu Kα_1 radiation (λ = 1.5406 Å) at room temperature. Data were collected in 0.02° increments at a rate of 1°/min.

2.7. Computational Studies. The Hirshfeld surfaces were generated using CrystalExplorer 17[28] for each symmetrically nonequivalent species in all three crystal structures, based on the experimental crystal structures. From there, two analyses were performed for studying the intermolecular interactions: quantitative analysis on Hirshfeld surfaces based on the "enrichment" of particular interactions above those expected based on chance, and ab initio calculations that directly looked at the pairwise interaction energies. Enrichment ratios were computed from Hirshfeld surfaces in order to understand how different interactions are favored. In order to expand the standard treatment[29] to a multicomponent system, the methodology was generalized as detailed in the Supporting Information. For the ab initio calculations, electrostatic potentials, generated using DFT methods as implemented in the Gaussian 09 software package[30] with the B3LYP functional and the 6-31G(d,p) basis set (DGDZVP for iodine), were calculated for each species and mapped onto the Hirshfeld surfaces. Interaction energy calculations were carried out from these data using CrystalExplorer 17. Grimme's D2 dispersion[31] and counterpoise BSSE corrections were used for all DFT calculations. Interaction energy calculations between pairs of molecules were carried out according to Turner et al. from these data. The cutoff distance for determining pairing was selected as 3.80 Å, and energy calculation results were compared by types and species. All ab initio calculations and mappings were conducted with Crystal Explorer 17 and its interface to the Gaussian program.

Table 1. Crystallographic Data

	dppe·*p*-F_4DIB$_{tri}$	dppe·*p*-F_4DIB$_{mono}$	dppe·3(*p*-F_4DIB)
formula	$C_{32}H_{24}F_4P_2I_2$	$C_{32}H_{24}F_4P_2I_2$	$C_{44}H_{24}F_{12}P_2I_6$
M_w	800.25	800.25	1603.97
space group	$P\bar{1}$	$P2_1/n$	$P\bar{1}$
a/Å	5.9963(11)	13.2235(10)	6.0112(8)
b/Å	11.9188(17)	5.8569(4)	13.0094(16)
c/Å	12.038(2)	19.3461(16)	15.4589(19)
α/deg	63.045(12)	90.00	92.620(8)
β/deg	87.203(19)	90.097(3)	98.623(8)
γ/deg	82.740(18)	90.00	91.589(8)
V/Å^3	760.7(2)	1498.3(2)	1193.3(3)
Z	1	2	1
D_c/g cm^{-3}	1.747	1.774	2.232
μ/mm^{-1}	2.218	2.252	4.051
transmission coeff.	0.698/1.00	0.71/0.90	0.912/1.00
no. of ref total	6462	39746	10040
no. of ref unique	3007	4617	4196
no. of ref obsd ($I > 2\sigma(I)$)	2873	4188	2910
no. of param.	181	181	289
R^a	0.0297	0.0196	0.0333
R_{all}	0.0312	0.0246	0.0552
$_wR^b$	0.0736	0.0387	0.0612
$_wR_{all}$	0.0751	0.0425	0.0687

$^aR_1 = \sum||F_o| - [F_c||/\sum|F_o|$. $^bwR_2 = \{\sum[w(F_o^2 - F_c^2)^2]/\sum[wF_o^2]^2\}^{1/2}$.

3. RESULTS AND DISCUSSION

While there are several crystals and cocrystals involving phosphorus-containing molecules exhibiting short intermolecular P···X (X = F, Cl, Br, I) contacts that meet the criteria for halogen bonding, only one targeted example has been published, by two separate groups.[23,24] As part of our effort to catalogue halogen bonded structures with a variety of X-acceptors, and in particular, expand upon the rare P···I crystal chemistry, we prepared cocrystals of *p*-F_4DIB and dppe. We have found that this combination does form cocrystals with strong P···I interactions, and that the cocrystal formed is dependent on the relative stoichiometry of the X-donor and X-acceptor with both 1:1 and 1:3 (acceptor:donor, respectively) cocrystals found. We also found that the 1:1 cocrystal forms as two polymorphic forms depending on the solvent used for crystallization: a triclinic form from pentane, and a monoclinic form from chloroform. All three cocrystals possess extended chains of alternating X-donors and X-acceptors, and the chains are linked through phenyl embraces in two or one of the other directions. Crystal data for all three cocrystals are displayed in Table 1, and halogen bonding distances and angles are displayed in Table 2.

3.1. Triclinic and Monoclinic Polymorphs of 1:1 dppe·*p*-F_4DIB. Two polymorphs of the 1:1 cocrystal of dppe and *p*-F_4DIB (dppe·*p*-F_4DIB$_{tri}$ and dppe·*p*-F_4DIB$_{mono}$) were obtained over the course of this study. Both polymorphs are built from extended chains of alternating X-donors and X-acceptors in a similar motif. The polymorphs are distinguished by the rotation of neighboring chains in the packing arrangement,

https://dx.doi.org/10.1021/acs.cgd.0c01129
Cryst. Growth Des. 2020, 20, 7460−7469

Table 2. Geometric Parameters for P···I Halogen Bonding

compound ID/REFCODE	P···I (Å)	P···I_{vdw} [a]	C–I···P (deg)	ref
dppe·*p*-F_4DIB_{tri}	3.1925(15)	0.845	172.930(9)	[b]
dppe·*p*-F_4DIB_{mono}	3.1732(5)	0.844	169.97(5)	[b]
dppe·3(*p*-F_4DIB)	3.251(2)	0.860	171.190(15)	[b]
EGOVOM	3.491(1)	0.924	170.73(8)	32
KIPCOE	3.376(1)	0.893	165.26(15)	23
KIPCOE01	3.3133(5)	0.877	165.33(4)	24
XIZCEQ	3.289(1)	0.870	163.06(11)	33

[a]Distance normalized to the vdw sum of phosphorus and iodine (I 1.98 Å; P 1.80 Å) [b]This paper.

presumably driven by phenyl embrace interactions linking the halogen bonded chains into the extended structures.

The triclinic polymorph has one formula unit per cell with half a molecule of both dppe and *p*-F_4DIB in the asymmetric unit, each situated about inversion centers at (1 1 0) and (1/2 1/2 1/2), respectively. Strong P···I halogen bonds link X-donor and X-acceptor molecules into steplike halogen bonded chains (Figure 1a) that run parallel to the [1 1 1] direction. This P···I interaction is especially worthy of comment, given the relative scarcity of P···I interactions reported in the literature (Table 2). The P···I halogen bond here (3.1925(15) Å) is shorter than those others reported in the literature, indicating a significant attractive interaction. The resulting halogen bonded chains are linked along the *a*-axis into layers by *ef* interactions between dppe molecules related by inversion symmetry (1/2 0 0). Each of the four phenyl rings of the dppe molecule serves as both edge-donors and as face-acceptors to form four *ef* interactions, each with a centroid-to-centroid distance of 5.014 Å. Chains related by (1/2 1/2 0) are very loosely associated through an *ff* interaction with an interplanar spacing of 3.991 Å, and a centroid-to-centroid distance of 4.909 Å.

The monoclinic polymorph contains two formula units per cell with half-molecules of both dppe and 1,4-F_4DIB in the asymmetric unit, each situated about inversion centers at (0 0 1/2) and (1/2 1/2 1/2), respectively. P···I halogen bonds again link X-donor and X-acceptor molecules into steplike halogen bonded chains (Figure 1b) that run parallel to the [1 0 0] direction. Similar to the triclinic polymorph, the key P···I interaction propagating the chains is relatively strong (3.1732(5) Å). As with the triclinic form, similar *ef* interactions link chains related by inversion symmetry (1/2 0 1/2) into layers along the *b*-direction. Each of the four phenyl rings of the dppe molecule serves as both edge-donors and as face-acceptors to form four *ef* interactions, each with a centroid-to-centroid distance of 4.839 Å. Unlike the triclinic polymorph, additional *ef* interactions occur between phenyl rings of chains related by *n*-glide symmetry to extend the structure into the third dimension along the *c*-direction. Each phenyl ring interacts with two symmetry-related rings to form a herringbone pattern with centroid-to-centroid distances of 5.021 and 5.474 Å, respectively.

Consequently, these subtle differences in the embracing result in distinctions in the packing arrangements (Figure 2). Embracing interactions (along the *a*-axis in the case of dppe·*p*-F_4DIB_{tri}, and along the *b*-axis in the case of dppe·*p*-F_4DIB_{mono}) link neighboring chains into layers. The stacking of consecutive layers in both polymorphs is shown in Figure 3. In the triclinic polymorph, the chains comprising the layers are well aligned in

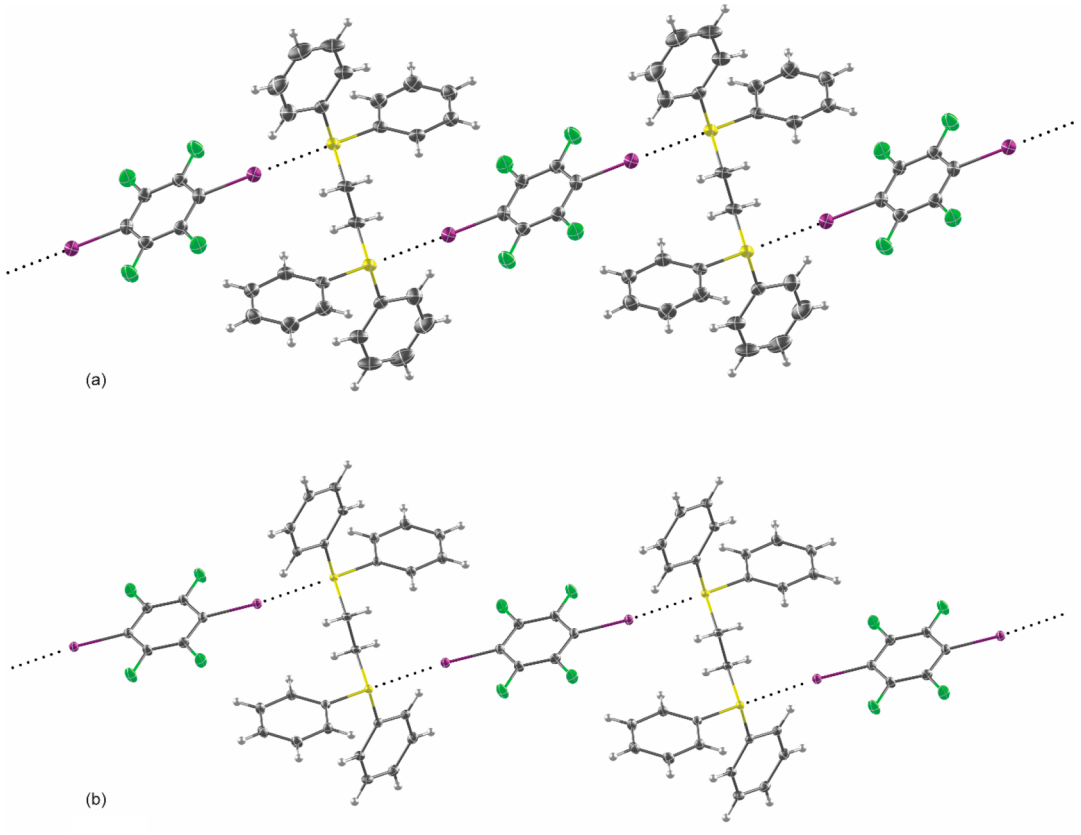

Figure 1. Stepped chains of dppe·*p*-F_4DIB_{tri} (a) and dppe·*p*-F_4DIB_{mono}(b).

https://dx.doi.org/10.1021/acs.cgd.0c01129
Cryst. Growth Des. 2020, 20, 7460−7469

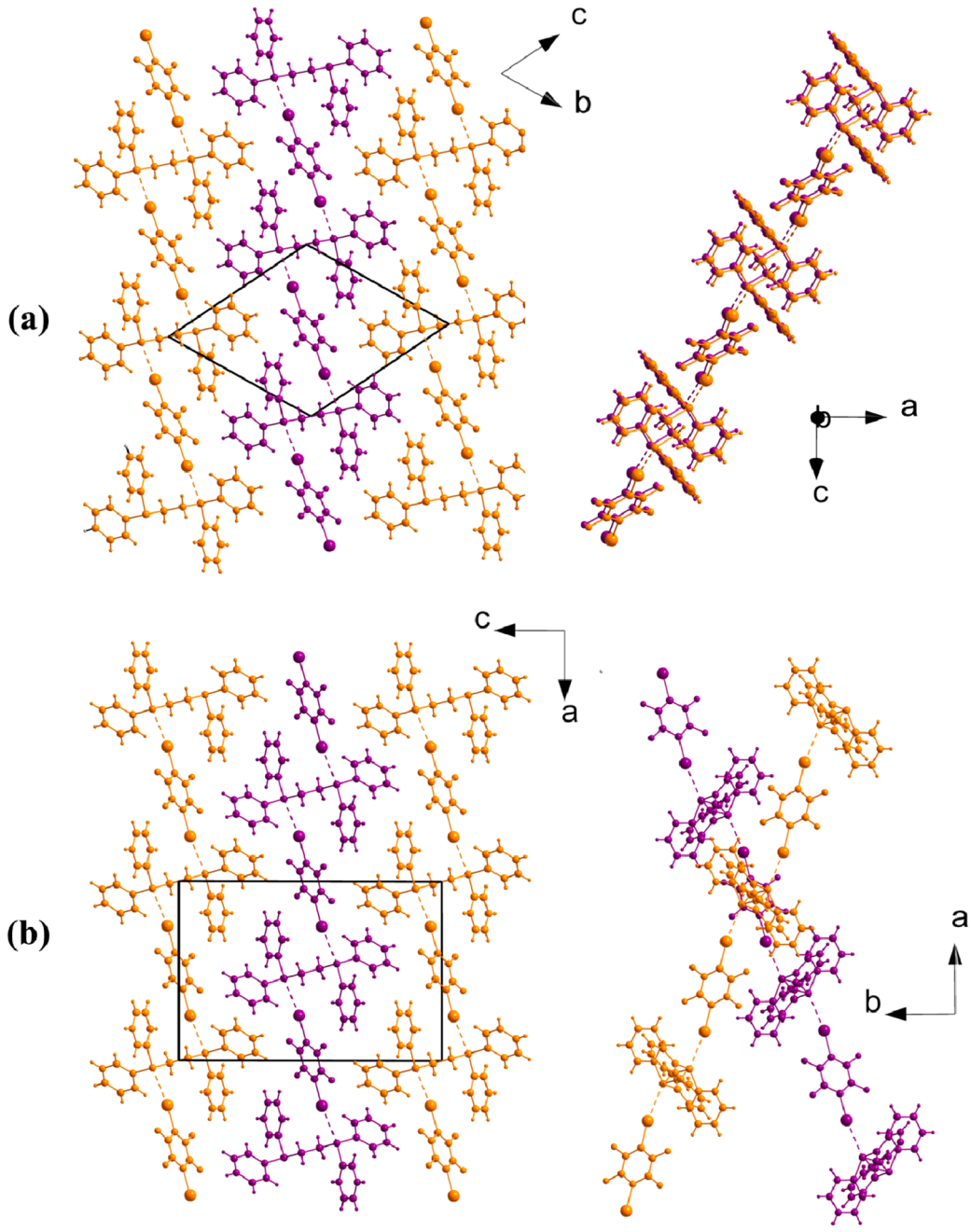

Figure 2. Layered structure ofdppe·*p*-F_4DIB_{tri} (a) and dppe·*p*-F_4DIB_{mono} (b). Left-hand images show the layers oriented toward their edges, whereas right-hand images show the orientation of constituent chains comprising the layers when oriented normal to the layer. Consecutive layers are denoted as orange and purple.

neighboring layers, and the layers are eclipsed. In the monoclinic polymorph, consecutive layers are rotated by about 40° to one another and offset in the alignment of the dppe and *p*-F_4DIB molecules. The offset between neighboring layers, in accordance with the *n*-glide symmetry, enables the additional *ef* embracing along the *c*-axis. In both polymorphs, weak C-H···F interactions (H···F = 2.52(2) Å in dppe·*p*-F_4DIB_{tri} and 2.5082(11) Å in dppe·*p*-F_4DIB_{mono}) between consecutive dppe and *p*-F_4DIB molecules within the chains serve to reinforce the chain along its direction of propagation and define the planar orientation of the *p*-F_4DIB linkers pinned by the opposing P···I halogen bonds. Subtle orientation differences of the *p*-F_4DIB molecules in the polymorphs are also manifested in the C−I···P angles.

In addition to the solvent dependence on the polymorphs' crystallization, we also studied their preferential synthesis through mechanochemistry (Figure 3). Mechanosynthesis of dppe·*p*-F_4DIB_{tri} from a 1:1 stoichiometric mixture of the constituent dppe and *p*-F_4DIB starting materials was found to proceed after just 30 s of grinding. The triclinic polymorph persisted exclusively for all grinding times under 10 min. After 15 min of grinding, a clean conversion to the monoclinic polymorph was observed. Polymorphic change during grinding has been known since the 1970s and typically involves a combination of thermodynamics and kinetics. Most often, the

https://dx.doi.org/10.1021/acs.cgd.0c01129
Cryst. Growth Des. 2020, 20, 7460−7469

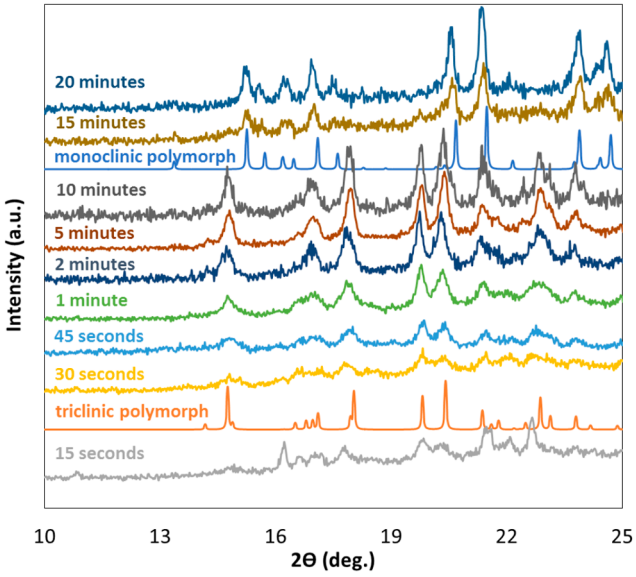

Figure 3. Mechanochemical synthesis of dppe·*p*-F_4DIB_{tri} and dppe·*p*-F_4DIB_{mono} polymorphs monitored by powder X-ray diffraction.

polymorphic transition occurs from a structure of lower density to a structure of higher density after grinding.[34,35] The improved packing associated with the higher density is generally considered indicative of a more stable structure. While the distinction is small in the present case (D_{tri} = 1.747 g/cm^3, D_{mono} = 1.774 g/cm^3), the general observation holds that the higher density polymorph is formed after extended grinding.

3.2. Structure of dppe·3(*p*-F_4DIB). Modifying the reaction stoichiometry to a 1:3 ratio of dppe:*p*-F_4DIB produced the corresponding 1:3 donor:acceptor cocrystal. This cocrystal contains half-molecules of dppe and *p*-F_4DIB situated on inversion centers at (1 0 1/2) and (1/2 1/2 1/2), respectively. An additional *p*-F_4DIB molecule is situated in a general position in the unit cell, accounting for the additional two *p*-F_4DIB molecules in the formula unit. Strong P···I halogen bonds again link X-donor and X-acceptor molecules into steplike X-bonded chains (Figure 4) that run along the *ab* face diagonal. Chains are linked into layers by *ef* interactions between dppe molecules related by inversion symmetry (1/2 1/2 0). Each of the four phenyl rings of the dppe molecule serve as both edge-donors and as face-acceptors to form four *ef* interactions, each with a centroid-to-centroid distance of 5.033 Å. Individually, these layers in the *ab* plane are essentially identical to those found in both of the 1:1 polymorphs.

The additional *p*-F_4DIB molecules in dppe·3(*p*-F_4DIB) decorate both sides of the P···I X-bonded chains through relatively weak I···I halogen bonds (I···I = 3.889(13) Å; C−I···I = 147.4(2)°) with the iodine atoms of the *p*-F_4DIB molecule that comprise the core of the P···I chains (Figure 4). These

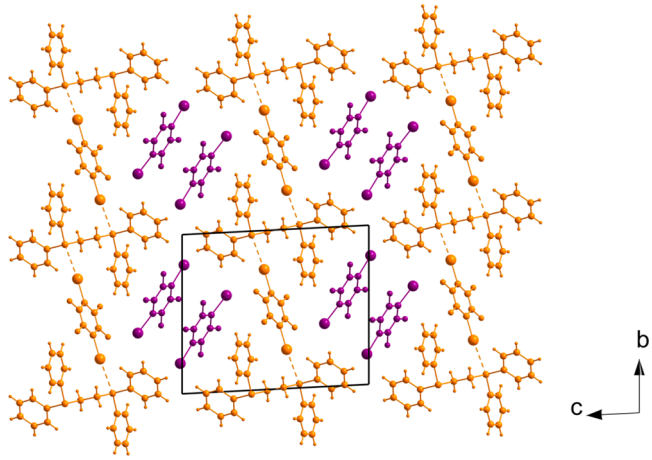

Figure 5. Connectivity of parallel layers (orange) of the embracing P···I chains through intermediate layers (purple) of extra *p*-F_4DIB molecules in dppe·3(*p*-F_4DIB).

extra *p*-F_4DIB molecules participate in a number of interactions that extend the structure along the *c*-axis (Figure 5), providing additional connectivity to the layers in the *ab* plane formed through the embracing interactions. Here, the layers are connected along the *c*-axis by I···π interactions involving a C−C bond of one of the phenyl rings of dppe (I···C distances of 3.576(10) and 3.631(10) Å). Furthermore, there is an offset π-stacking interaction between the *p*-F_4DIB molecules (shortest C···C distance = 3.552(14) Å) that also connects the *ab* layers along the *c*-axis. This creates somewhat of a hybrid situation to what was encountered in the 1:1 polymorphs. The layers in the *ab* plane are aligned with one

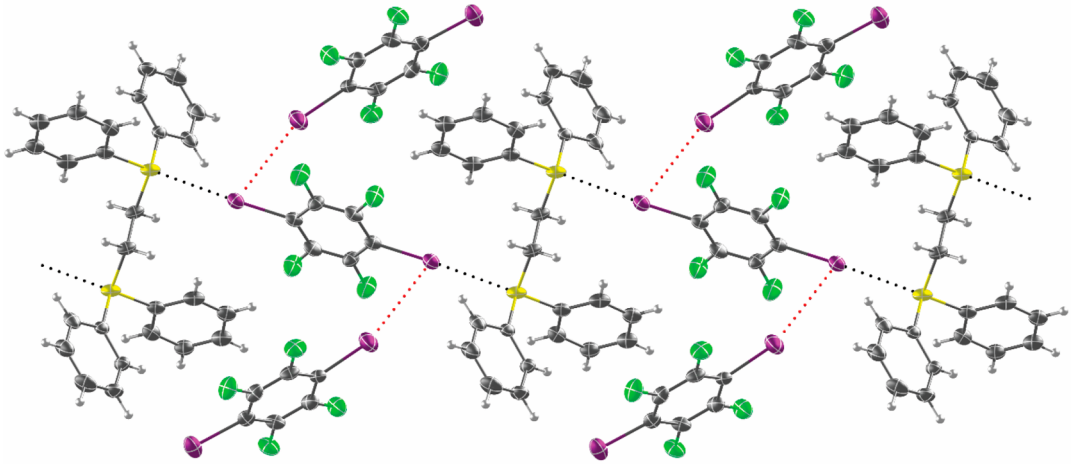

Figure 4. Decorated halogen bonded chain of dppe·3(*p*-F_4DIB).

https://dx.doi.org/10.1021/acs.cgd.0c01129
Cryst. Growth Des. 2020, 20, 7460−7469

another, similar to what was observed in the triclinic polymorph. The extra *p*-F_4DIB decorations, however, perform a similar role to the rotated layers of monoclinic polymorph, enabling additional intermolecular interactions (embraces in the case of dppe·*p*-F_4DIB_{mono}, and pi interactions in the case of dppe·3(*p*-F_4DIB)) that extend the long-range structures into frameworks.

3.3. Mechanochemical Synthesis and Thermal Analysis. In addition to the time-dependent mechanochemical synthesis of the 1:1 polymorphs described above, we also studied the mechanochemical synthesis of the 1:1 and 1:3 cocrystals as a function of reaction composition. A 5 min grinding time was employed to ensure the reactions reached completion to give satisfactorily crystalline products. In this way, the phase stability of the triclinic 1:1 cocrystal and the 1:3 cocrystal was determined (Figure 6). The triclinic 1:1 cocrystal

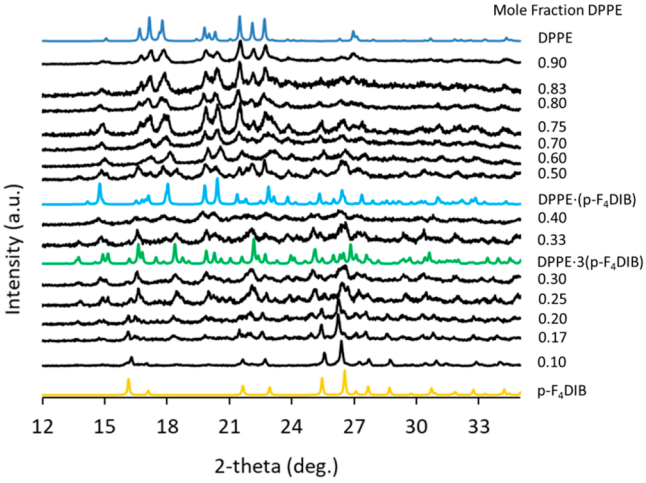

Figure 6. Stoichiometric dependence of phase formation by mechanochemistry measured by powder XRD.

is stable for DPPE mole fractions ranging from 0.83 to 0.33 and was judged to be phase pure (free from unreacted DPPE or 1:3 cocrystal) from 0.75 to 0.50. For DPPE mole fractions of 0.5 to 0.33, a mixture of the 1:1 and 1:3 cocrystals was obtained. The 1:3 cocrystal was stable as a phase pure product for DPPE mole fractions of 0.33 to 0.20. No significant amount of the 1:3 cocrystal was obtained below a DPPE mole fraction of 0.17. Further, the mechanochemical experiments did not indicate the presence of other cocrystals beyond the 1:1 and 1:3 stoichiometries.

Preparation of phase-pure materials by controlling the stoichiometry and grinding time during mechanochemical synthesis enabled a systematic thermal analysis by DSC/TGA (Figure 7a–c) and corroborating melting point measurements using a standard melting point apparatus (Figure 7d). Thermally driven mass loss occurs from the 1:1 cocrystals over a range of 100–180 °C, and from the 1:3 cocrystal, over a range 80–220 °C. In all cases, this corresponds to the loss of the *p*-F_4DIB molecules, and the observed mass loss is in good agreement with that calculated from 1:1 and 1:3 cocrystal compositions (Table 3). The melting points of samples prepared by mechanochemistry in the phase pure stoichiometric regions corresponding to 1:1 cocrystals and 1:3 cocrystals and measured by the melting point apparatus are consistent with those measured by DSC (Table 3). In this way, measuring the melting point as a function of reaction stoichiometry can be an informative means of identifying the presence of different cocrystals, where significant changes in slope accompany the formation of different cocrystal phases. No thermally driven polymorphic transition was observed for the 1:1 cocrystal polymorphs, and the two possess similar melting points and similar densities, suggesting only a small energy difference between the forms. The eventual formation of the monoclinic polymorph from extended mechanochemical grinding of the initially formed triclinic polymorph coupled with its slightly higher melting point and density suggests it may hold a slightly higher stability.

3.4. Enrichment Ratios. Hirshfeld surfaces are used to partition space in a crystalline environment in order to extract information about the intermolecular interactions. Assigning surface area based on closest elements yields a quantitative descriptor of the intermolecular contacts, called Hirshfeld surface contacts.[29] The "enrichment ratio" (ER) is a derived descriptor from Hirshfeld surface contacts by Jelsch et al. The ER is calculated by comparing the frequency of the intermolecular atom contacts actually found within a crystal against the frequency that would be expected if there were no energetic preferences between the possible interactions. The ER_{XY} values for a particular pair of atoms X and Y will be greater than 1 if the interaction tends to occur more often than chance, whereas those less than 1 indicate contacts which are disfavored. For each crystal structure, three key quantitative descriptors are reported (Table S1): Hirshfeld surface contacts (normalized), random contacts, and enrichment ratios computed from the Hirshfeld surface contacts and random contacts. Compared to ab initio calculations, the analysis of these descriptors does not rely on accuracy of the level of theory used and offers direct insight to crystal packing and intermolecular motifs.

Table 4 lists the largest ERs for the three cocrystals (complete atom–atom contact data in Table S1, Supporting Information). The I···H, I···P, H···F, and F···F contacts have the highest ERs. The hydrogen–halide contacts H···F and H···I contact enrichments are greater than unity and relatively consistent across the compounds. This favorable interaction is expected due to simple electrostatics. Surprisingly, the ER for F···F contacts is greater than that of H···F and is also consistent across changes in the total surface area of fluorine. This is higher than was previously observed in a study of several aliphatic and aromatic hydrofluorocarbons.[36]

It has been suggested that, when the "random contacts" of a compound are lower than 0.9%, the ER may not be meaningful.[29] In these crystals, phosphorus occupies less than 2% of the surface area, leading to the calculated random contacts between that element and iodine to be 0.4%. However, the I···P contact is associated with a relatively high interaction energy value (around 24 kJ/mol at this level of theory), even though the surface contact area is exceedingly small. Therefore, we report the ER values (4.54, 8.01, and 8.09, respectively) in the three cocrystals, because they clearly show that phosphorus has a very high tendency to form I···P contacts–halogen bonds–though the magnitude of this value may be distorted by the low phosphorus contribution to the molecular surface.

All of the cocrystals show multiple variations of the phenyl embrace, including those between phenyl rings on adjacent phosphines (e.g., *ff* embraces) and those between phosphine phenyl rings and the fluorinated benzenes of the halogen bond donor (e.g., $ff_{H\text{-}F}$ embraces). The difference in the extent and

https://dx.doi.org/10.1021/acs.cgd.0c01129
Cryst. Growth Des. 2020, 20, 7460–7469

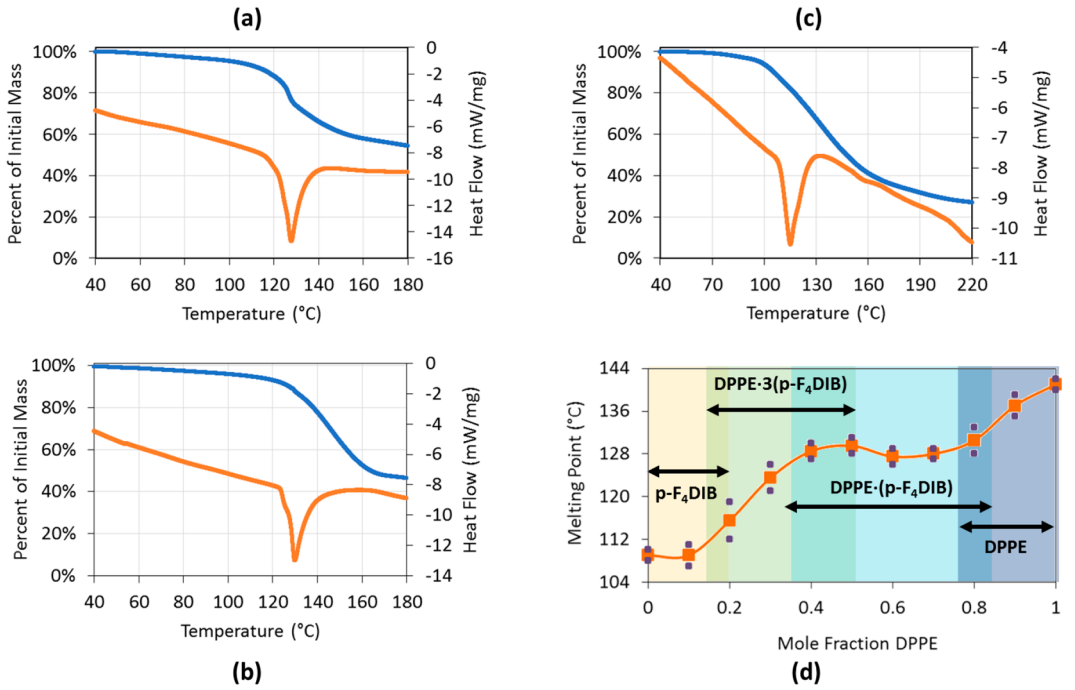

Figure 7. (a) DSC/TGA of dppe·*p*-F_4DIB_{tri}. (b) DSC/TGA of dppe·*p*-F_4DIB_{mono}. (c) DSC/TGA of dppe·3(*p*-F_4DIB). (d) Melting point as a function of mechanochemical composition measured with the melting point apparatus (average melting point shown as orange squares, range denoted by purple squares). For DSC/TGA data, DSC is shown as the orange lines and TGA as the blue lines.

Table 3. Thermal Data for All Three Phosphine Structures Measured by DSC/TGA

cocrystal	melting point onset (°C)	melting point peak (°C)	observed mass loss (%)	calculated mass loss of organoiodine (%)
dppe·*p*-F_4DIB_{tri}	121	128	45.7	50.2
dppe·*p*-F_4DIB_{mono}	123	130	53.6	50.2
dppe·3(*p*-F_4DIB)	109	116	73.1	75.2

energetic importance of these interactions can be understood from a quantitative aspect. The C···H contacts in Table 4 primarily correspond to *vf* and *ef* phenyl embraces between phosphine acceptors, whereas C···C contacts are due to *ff* and $ff_{H\text{-}F}$ embraces. The I···C contacts are also due to a specific phenyl embrace, that of the $vf_{H\text{-}F}$ variety, though it is also a π-to-I halogen bond. Hirshfeld surface contacts show that dppe·*p*-F_4DIB_{mono} has significantly less C···C contact area as compared to dppe·*p*-F_4DIB_{tri} and especially dppe·3(*p*-F_4DIB) (Table S1). Indeed, the ER of C···C for this compound is significantly less than unity, whereas the H···C ER is the largest of the three. Enrichment ratio analysis suggests that dppe·*p*-F_4DIB_{mono} prefers *vf* embraces, whereas its polymorph, dppe·*p*-F_4DIB_{tri}, and the organohalide-rich dppe·3(*p*-F_4DIB) prefer *ff* embraces. For I···P interactions, the ER of the organohalide-rich structure, dppe·3(*p*-F_4DIB), is about half that in the other two. Considering that the surface portion occupied by iodine is twice as large in dppe·3(*p*-F_4DIB) as in the other two structures (Table S1), and the space for I···P interaction is similarly limited in all three structures, it cannot be concluded that the I···P contact is less favored in dppe·3(*p*-F_4DIB). We also conclude that enrichment ratio analysis is best at understanding whether an interaction is favored or disfavored in the packing, but not a good indicator of the strength of the interaction.

3.5. Interaction Energies and Framework Energy Diagrams. Ultimately, the stability of the crystals is dependent upon the strength of intermolecular interactions between the molecular components. Here, the most important of the interaction energies within each crystal, as calculated by CrystalExplorer, were broken down into component energies and analyzed by interaction type between adjacent molecular pairs (Tables 5−7). The pairs were defined as a central molecule and each strongly interacting adjacent molecule. The simple energy decomposition scheme used here (eq 1) is as follows

$$E_{tot} = E_{ele} + E_{pol} + E_{dis} + E_{rep} \quad (1)$$

where E_{tot} is the total energy, E_{ele} is the electrostatic energy, E_{pol} is the polarization energy, E_{dis} is the dispersive, and E_{rep} is the exchange−repulsion energy. Note that E_{tot} is the sum of the scaled components using model appropriate scaling factors. The individual components are not scaled.

Table 4. Enrichment Ratios Listed by Interaction Type

compound	C···H	I···H	C···C	I···C	I···P	H···F	F···F
dppe·3(*p*-F_4DIB)	1.11	1.44	1.38	1.06	4.54	1.20	1.44
dppe·*p*-F_4DIB_{mono}	1.41	1.23	0.30	0.74	8.01	1.25	1.44
dppe·*p*-F_4DIB_{tri}	1.17	1.21	1.02	0.60	8.69	1.18	1.33

https://dx.doi.org/10.1021/acs.cgd.0c01129
Cryst. Growth Des. 2020, 20, 7460−7469

Table 5. Interaction Energies between a Central Molecule and an Adjacent Molecule Broken Down by Type of Contact in Crystals of dppe·3(*p*-F_4DIB)[a]

central	paired	primary contact	$D_{norm} < 0$	N	R	E_{ele}	E_{pol}	E_{dis}	E_{rep}	E_{tot}
dppe	dppe	*vf* embrace and translational face-to-face	n	2	6.01	−11.8	−2.3	−62.9	29.4	−50.8
dppe	dppe	H···H (edge-to-edge)	n	2	15.46	−0.6	−0.1	−8.2	4.8	−4.9
DIB-a	dppe	I···π (distorted phenyl *ff*) and F···H	n	1	7.88	−5.9	−0.8	−36.7	18.8	−27.2
DIB-a	dppe	I···C (*vf*)	yes	1	11.09	−7.9	−1	−14.5	17.1	−11.1
DIB-a	dppe	I···phenyl π (distorted *vf*)	n	1	10.26	−1.7	−0.4	−8.4	3.7	−7.1
DIB-a	dppe	F···H	yes	1	10.9	−2	−0.2	−9.3	5.4	−7
DIB-a	dppe	I···H	n	1	11.63	−4.3	−0.1	−8.2	11.3	−4.8
DIB-a	dppe	I···H	yes	1	10.8	−1.7	−0.1	−6	4	−4.6
DIB-a	dppe	I···H	n	1	8.82	−0.9	−0.1	−7.4	5	−4.4
DIB-b	dppe	I···π and F···H	n	2	7.09	−8.1	−0.8	−37.5	27.3	−24.9
DIB-b	dppe	I···P	yes	2	7.24	−59.5	−5.2	−25	103.8	−24.4
DIB-a	DIB-a	C···C (face-to-face)	n	1	4.18	−8.6	−0.9	−44.4	34.2	−27.3
DIB-a	DIB-a	F···F (side-to-side)	n	2	6.01	−3.6	−0.3	−20.4	8.4	−16.6
DIB-a	DIB-a	F···F (edge-to-edge)	yes	1	7.26	0.7	−0.1	−10.3	3.2	−6.5
DIB-b	DIB-b	F···F (side-to-side)	n	2	6.01	−3.4	−0.3	−19.1	7	−16.1
DIB-a	DIB-b	I···I	yes	1	6.25	−12.7	−0.4	−15.4	27.4	−10.2
DIB-a	DIB-b	I···F	yes	1	7.86	−2.9	−0.1	−8.2	7.5	−5.7

[a]N refers to the number of the molecules in the cluster; R refers to the molecular centroid-to-centroid distance (in Å). All interaction energies are expressed in kJ/mol.

Table 6. Interaction Energies between a Central Molecule and an Adjacent Molecule Broken Down by Type of Contact in Crystals of dppe·*p*-F_4DIB$_{mono}$[a]

central	paired	primary contact	$D_{norm} < 0$	N	R	E_{ele}	E_{pol}	E_{dis}	E_{rep}	E_{tot}
dppe	dppe	*vf* embrace	yes	2	5.89	−18.8	−3	−76.3	49.7	−57.9
dppe	dppe	*vf* embrace	n	4	12.09	−3.6	−0.8	−16.5	11.2	−11.8
dppe	dppe	H···H (edge-to-edge)	n	4	12.12	−1.5	−0.4	−17.2	9.6	−10.9
DIB	dppe	I···P and F···H	yes	2	7.25	−67.3	−5.6	−25.4	121.1	−22.6
DIB	dppe	I···π and F···H	n	2	7.25	−8.5	−0.7	−34.6	27.9	−22.4
DIB	dppe	C···H, I···H	n	2	9.7	−2	−0.3	−16.9	12.3	−9.5
DIB	dppe	H···F	n	2	11.35	−1.1	−0.1	−4.9	2.3	−4.1
DIB	DIB	F···F (side-to-side)	n	2	5.89	−3.1	−0.3	−20	7.2	−16.4

[a]N refers to the number of the molecules in the cluster; R refers to the molecular centroid-to-centroid distance (in Å). All interaction energies are expressed in kJ/mol.

Table 7. Interaction Energies between a Central Molecule and an Adjacent Molecule Broken Down by Type of Contact in Crystals of dppe·*p*-F_4DIB$_{tri}$[a]

central	paired	primary contact	$D_{norm} < 0$	N	R	E_{ele}	E_{pol}	E_{dis}	E_{rep}	E_{tot}
dppe	dppe	*vf* embrace	n	2	6	−11.3	−2.3	−61.8	30	−48.9
dppe	dppe	face-to-face and edge-to-edge embrace	n	2	12.65	−3.6	−0.5	−26.6	13.9	−18.8
dppe	dppe	H···phenyl π	n	2	12.04	−1.3	−0.8	−14.1	5.6	−10.7
dppe	dppe	H···H	n	2	11.92	−1.1	−0.3	−15.8	9.5	−9.3
dppe	dppe	H···H	n	2	13.71	−0.2	−0.1	−6.1	2.8	−3.9
dppe	dppe	H···H	n	2	15.81	0.4	−0.1	−1.7	0.1	−1
DIB	DIB	F···F (side-to-side)	n	2	6	−3.9	−0.3	−19.7	8.8	−16
dppe	DIB	I···π (distorted phenyl *ff*) and F···H	yes (F···H)	2	6.74	−9.6	−1	−43.6	34.6	−27.5
dppe	DIB	I···P	yes	2	7.14	−69.2	−5.8	−25.6	122.7	−24
dppe	DIB	F···H	n	2	10.34	−0.2	−0.1	−8.5	2.2	−6.3
dppe	DIB	I···H	n	2	10.93	−1.6	−0.1	−8.3	6.9	−4.8

[a]N refers to the number of the molecules in the cluster; R refers to the molecular centroid-to-centroid distance (in Å). All interaction energies are expressed in kJ/mol.

In each of the structures, the *vf* phenyl embraces in dppe-dppe pairs are the strongest interaction, with total interaction energies of −50.8, −57.9, and 48.9 kJ/mol for dppe·3(*p*-F_4DIB), dppe·*p*-F_4DIB$_{mono}$, and dppe·*p*-F_4DIB$_{tri}$, respectively. Unsurprisingly, in each case, total energies are dominated by the very large dispersion energy terms. This agrees well with enrichment ratio analysis that suggests dppe·*p*-F_4DIB$_{mono}$ prefers C···H contacts the most (*vf* embraces). We also identify some other strong interactions including the iodine···π interactions (ff_{AD} overlaps) in dppe-F_4DIB pairs, and the iodine···phosphorus interactions in F_4DIB-dppe pairs.

Interestingly, we find that short contacts (atom distance < sum of vdW radii, or $D_{norm} < 0$) do not always indicate a strong intermolecular attraction. For example, the short F···H contact

https://dx.doi.org/10.1021/acs.cgd.0c01129
Cryst. Growth Des. 2020, 20, 7460−7469

in dppe·3(p-F_4DIB) only shows a total energy of −7 kJ/mol and the short I···H contact is only −4.6 kJ/mol. On the other hand, pairs that do not possess short contacts can be of extremely high dispersion energy, which results in a high total interaction energy, such as the *vf* phenyl embrace.

Framework energy diagrams of each crystal are given in Figures S3−S5, where the cylinder size correlates to the strength of interaction. From the diagrams, we report that strong electrostatic energy contributions to the total interaction energies were observed in all three crystal structures as a result of I···P interactions. The I···P electrostatic interaction contributes to the overall energy framework significantly and, in particular, forms the framework in one dimension, whereas the dispersion forces including *vf* phenyl embrace and I···π interaction (ff_{AD} embrace) complete the three-dimensional framework.

4. CONCLUSIONS

A series of cocrystals based on dppe and p-F_4DIB in 1:1 and 1:3 ratios have been prepared and their structures characterized by single-crystal X-ray diffraction and computational techniques. All of the structures feature rare P···I halogen bonds that connect the donor and acceptor molecules into infinite chains and significantly expand the class of compounds based on the P···X motif. The structures also feature complementary phenyl embraces that create two-dimensional layers from the halogen bonded chains and can further extend the structures into three-dimensional frameworks. The 1:1 composition presents itself as two different polymorphs, with differences in the orientation of layers in the packing arrangements influenced by variations in phenyl embracing. The 1:3 cocrystal incorporates structural features of both of the 1:1 polymorphs, with the additional p-F_4DIB molecules decorating the core P···I chains, and participating in π-stacking and I···π interactions. Synthetic control of all the phases can be achieved from solution synthesis by solvent and stoichiometric considerations, and from mechanochemical synthesis by varying the stoichiometry and grinding time. Thermal analysis indicates similar melting and decomposition behavior of the 1:1 polymorphs. Decomposition of the 1:1 and 1:3 cocrystals via loss of p-F_4DIB molecules occurs approaching and throughout their respective melting points. Additionally, the work demonstrates that green techniques such as solvent-free mechanosynthesis, coupled with simple melting point measurements, can be used to conveniently screen phase space to identify candidate cocrystals for crystallographic analysis.

Computational studies with Hirshfeld surface analysis and ab intio calculations were conducted to better understand how different types of interactions contributed to crystal packing and structural stability. Hirshfeld surface and enrichment ratio analysis suggests that dppe·p-F_4DIB_{mono} prefers *vf* and $vf_{H\text{-}F}$ phenyl embraces, its polymorph dppe·p-F_4DIB_{tri} shows both strong $vf_{H\text{-}F}$ and *ff* embraces, and the organohalide-rich dppe·3(p-F_4DIB) highly favors $ff_{H\text{-}F}$ embraces. This agrees well with detailed analysis with pairwise interaction energies from ab initio calculations. Further, energetic framework diagrams were plotted based on ab initio calculations. The diagrams suggest that strong electrostatic interactions were observed in one dimension of all three crystal structures, as a result of iodine··· phosphorus interactions, and dispersion forces contribute across the other two dimensions.

■ ASSOCIATED CONTENT

Supporting Information

The Supporting Information is available free of charge at https://pubs.acs.org/doi/10.1021/acs.cgd.0c01129.

A complete list of Hirschfeld contacts and enrichment ratios can be found in Table S1. Figures showing the energy electrostatic, dispersion, and total energy frameworks for each compound looking down the *a*-, *b*-, and *c*-axes may be found in Figures S3−S5, respectively (PDF)

Accession Codes

CCDC 2021949−2021951 contain the supplementary crystallographic data for this paper. These data can be obtained free of charge via www.ccdc.cam.ac.uk/data_request/cif, or by emailing data_request@ccdc.cam.ac.uk, or by contacting The Cambridge Crystallographic Data Centre, 12 Union Road, Cambridge CB2 1EZ, UK; fax: +44 1223 336033.

■ AUTHOR INFORMATION

Corresponding Author

William T. Pennington − *Department of Chemistry, Clemson University, Clemson, South Carolina 29634, United States*; Email: billp@clemson.edu

Authors

Adam M. Siegfried − *Department of Chemistry, Clemson University, Clemson, South Carolina 29634, United States*

Hadi D. Arman − *Department of Chemistry, Clemson University, Clemson, South Carolina 29634, United States*

Khadijatul Kobra − *Department of Chemistry, Clemson University, Clemson, South Carolina 29634, United States*

Kunhuan Liu − *Department of Chemistry, Furman University, Greenville, South Carolina 29613, United States*

Andrew J. Peloquin − *Department of Chemistry, Clemson University, Clemson, South Carolina 29634, United States*; orcid.org/0000-0002-7535-2049

Colin D. McMillen − *Department of Chemistry, Clemson University, Clemson, South Carolina 29634, United States*; orcid.org/0000-0002-7773-8797

Timothy Hanks − *Department of Chemistry, Furman University, Greenville, South Carolina 29613, United States*

Complete contact information is available at: https://pubs.acs.org/10.1021/acs.cgd.0c01129

Funding

The material is based upon work supported in part by the National Science Foundation under award number CHE-1757706 and by the Petroleum Research Fund under award number PRF no. 54873-UR7.

Notes

The authors declare no competing financial interest.

■ REFERENCES

(1) Desiraju, G. R.; Ho, P. S.; Kloo, L.; Legon, A. C.; Marquardt, R.; Metrangolo, P.; Politzer, P.; Resnati, G.; Rissanen, K. Definition of the Halogen Bond (IUPAC Recommendations 2013). *Pure Appl. Chem.* **2013**, *85*, 1711−1713.

(2) Thekkeppat, N. P.; Lakshmipathi, M.; Jalilov, A. S.; Das, P.; Peedikakkal, A. M. P.; Ghosh, S. Combining Optical Properties with Flexibility in Halogen-Substituted Benzothiazole Crystals. *Cryst. Growth Des.* **2020**, *20*, 3937−3943.

(3) Pancholi, J.; Beer, P. D. Halogen Bonding Motifs for Anion Recognition. *Coord. Chem. Rev.* **2020**, *416*, 213281.

(4) Pizzi, A.; Pigliacelli, C.; Bergamaschi, G.; Gori, A.; Metrangolo, P. Biomimetic Engineering of the Molecular Recognition and Self-Assembly of Peptides and Proteins via Halogenation. *Coord. Chem. Rev.* **2020**, *411*, 213242.
(5) Yang, Z.; Xu, C.; Li, W.; Mao, Z.; Ge, X.; Huang, Q.; Deng, H.; Zhao, J.; Gu, F. L.; Zhang, Y.; Chi, Z.; et al. Boosting the Quantum Efficiency of Ultralong Organic Phosphorescence up to 52% via Intramolecular Halogen Bonding. *Angew. Chem.* **2020**, *132*, 17604−17608.
(6) Tang, R.; Zhou, S.; Li, H.; Chen, R.; Zhang, L.; Yin, L. Halogen Bonding Induced Aqueously Stable CsPbBr3@MOFs-Derived Co3O4/N-Doped-C Heterostructure for High-Performance Photoelectrochemical Water Oxidation. *Appl. Catal., B* **2020**, *265*, 118583.
(7) Cavallo, G.; Metrangolo, P.; Milani, R.; Pilati, T.; Priimagi, A.; Resnati, G.; Terraneo, G. The Halogen Bond. *Chem. Rev.* **2016**, *116*, 2478−2601.
(8) Padgett, C. W.; Walsh, R. D.; Drake, G. W.; Hanks, T. W.; Pennington, W. T. New Conformations and Binding Modes in Halogen-Bonded and Ionic Complexes of 2,3,5,6-Tetra(2′-Pyridyl)-Pyrazine. *Cryst. Growth Des.* **2005**, *5*, 745−753.
(9) Padgett, C. W.; Pennington, W. T.; Hanks, T. W. Conformations and Binding Modes of 2,3,5,6-Tetra(2′-Pyridyl)Pyrazine. *Cryst. Growth Des.* **2005**, *5*, 737−744.
(10) Crihfield, A.; Hartwell, J.; Phelps, D.; Walsh, R. B.; Harris, J. L.; Payne, J. F.; Pennington, W. T.; Hanks, T. W. Crystal Engineering through Halogen Bonding. 2. Complexes of Diacetylene-Linked Heterocycles with Organic Iodides. *Cryst. Growth Des.* **2003**, *3*, 313−320.
(11) Walsh, R. B.; Padgett, C. W.; Metrangolo, P.; Resnati, G.; Hanks, T. W.; Pennington, W. T. Crystal Engineering through Halogen Bonding: Complexes of Nitrogen Heterocycles with Organic Iodides. *Cryst. Growth Des.* **2001**, *1*, 165−175.
(12) Rimmer, E. L.; Bailey, R. D.; Hanks, T. W.; Pennington, W. T. Complexes of Acridine and 9-Chloroacridine with I2: Formation of Unusual I6 Chains through Charge-Transfer Interactions Involving Amphoteric I2. *Chem. - Eur. J.* **2000**, *6*, 4071−4081.
(13) Bailey, R. D.; Hook, L. L.; Watson, R. P.; Hanks, T. W.; Pennington, W. T. Tetraiodoethylene: A Supramolecular Host for Lewis Base Donors. *Cryst. Eng.* **2000**, *3*, 155−171.
(14) Phelps, D.; Crihfield, A.; Hartwell, J.; Hanks, T. W.; Pennington, W. T.; Bailey, R. D. Synthesis of Polydiacetylene Charge-Transfer Complexes. *Mol. Cryst. Liq. Cryst. Sci. Technol., Sect. A* **2000**, *354*, 523−530.
(15) Jay, J. I.; Padgett, C. W.; Walsh, R. D. B.; Hanks, T. W.; Pennington, W. T. Noncovalent Interactions in 2-Mercapto-1-Methylimidazole Complexes with Organic Iodides. *Cryst. Growth Des.* **2001**, *1*, 501−507.
(16) Arman, H. D.; Gieseking, R. L.; Hanks, T. W.; Pennington, W. T. Complementary Halogen and Hydrogen Bonding: Sulfur iodine Interactions and Thioamide Ribbons. *Chem. Commun.* **2010**, *46*, 1854−1856.
(17) Arman, H. D.; Rafferty, E. R.; Bayse, C. A.; Pennington, W. T. Complementary Selenium···iodine Halogen Bonding and Phenyl Embraces: Cocrystals of Triphenylphosphine Selenide with Organoiodides. *Cryst. Growth Des.* **2012**, *12*, 4315−4323.
(18) Walsh, R. D.; Smith, J. M.; Hanks, T. W.; Pennington, W. T. Computational and Crystallographic Studies of Pseudo-Polyhalides. *Cryst. Growth Des.* **2012**, *12*, 2759−2768.
(19) Kobra, K.; O'Donnell, S.; Ferrari, A.; McMillen, C. D.; Pennington, W. T. Halogen Bonding and Triiodide Asymmetry in Cocrystals of Triphenylmethylphosphonium Triiodide with Organoiodines. *New J. Chem.* **2018**, *42*, 10518−10528.
(20) Riel, A. M. S.; Jessop, M. J.; Decato, D. A.; Massena, C. J.; Nascimento, V. R.; Berryman, O. B. Experimental Investigation of Halogen-Bond Hard-Soft Acid-Base Complementarity. *Acta Crystallogr., Sect. B: Struct. Sci., Cryst. Eng. Mater.* **2017**, *73*, 203−209.
(21) Groom, C. R.; Bruno, I. J.; Lightfoot, M. P.; Ward, S. C. The Cambridge Structural Database. *Acta Crystallogr., Sect. B: Struct. Sci., Cryst. Eng. Mater.* **2016**, *72*, 171−179.
(22) CSD REFCODES for P···X-C (atomic coordinates, R < 10%, nondisordered, single-crystal only, for P···X < vdw sum - 0.1 Å, P···X-C (°) 135−180): (X = I) EGOVOM, KIPCOE, KIPCOE01-04, XIZCEQ; (X = Br): OJEJET, SINVIU10, TUCVEU; (X = Cl): BUWXUO, SINVOA; (X = F): AGITUI.
(23) Xu, Y.; Huang, J.; Gabidullin, B.; Bryce, D. L. A Rare Example of a Phosphine as a Halogen Bond Acceptor. *Chem. Commun.* **2018**, *54*, 11041−11043.
(24) Lisac, K.; Topić, F.; Arhangelskis, M.; Cepić, S.; Julien, P. A.; Nickels, C. W.; Morris, A. J.; Friščić, T.; Cinčić, D. Halogen-Bonded Cocrystallization with Phosphorus, Arsenic and Antimony Acceptors. *Nat. Commun.* **2019**, *10*, 10.
(25) Friščič, T.; Jones, W. Recent Advances in Understanding the Mechanism of Cocrystal Formation via Grinding. *Cryst. Growth Des.* **2009**, *9*, 1621−1637.
(26) Dance, I.; Scudder, M. Molecules Embracing in Crystals. *CrystEngComm* **2009**, *11*, 2233−2247.
(27) Sheldrick, G. M. Crystal Structure Refinement with SHELXL. *Acta Crystallogr., Sect. C: Struct. Chem.* **2015**, *71*, 3−8.
(28) Turner, M. J.; McKinnon, J. J.; Wolff, S. K.; Grimwood, D. J.; Spackman, P. R.; Jayatilaka, D.; Spackman, M. A. *Crystal Explorer17*; University of Western Australia; 2017. http://hirshfeldsurface.net.
(29) Jelsch, C.; Ejsmont, K.; Huder, L. The Enrichment Ratio of Atomic Contacts in Crystals, an Indicator Derived from the Hirshfeld Surface Analysis. *IUCrJ* **2014**, *1*, 119−128.
(30) Frisch, M. J.; Trucks, G. W.; Schlegel, H. B.; Scuseria, G. E.; Robb, M. A.; Cheeseman, J. R.; Scalmani, G.; Barone, V.; Petersson, G. A.; Nakatsuji, H.; Li, X.; Caricato, M.; Marenich, A.; Bloino, J.; Janesko, B. G.; Gomperts, R.; Mennucci, B.; Hratchian, H. P.; Ortiz, J. V.; Izmaylov, A. F.; Sonnenberg, J. L.; Williams-Young, D.; Ding, F.; Lipparini, F.; Egidi, F.; Goings, J.; Peng, B.; Petrone, A.; Henderson, T.; Ranasinghe, D.; Zakrzewski, V. G.; Gao, J.; Rega, N.; Zheng, G.; Liang, W.; Hada, M.; Ehara, M.; Toyota, K.; Fukuda, R.; Hasegawa, J.; Ishida, M.; Nakajima, T.; Honda, Y.; Kitao, O.; Nakai, H.; Vreven, T.; Throssell, K.; Montgomery, J. A., Jr.; Peralta, J. E.; Ogliaro, F.; Bearpark, M.; Heyd, J. J.; Brothers, E.; Kudin, K. N.; Staroverov, V. N.; Keith, T.; Kobayashi, R.; Normand, J.; Raghavachari, K.; Rendell, A.; Burant, J. C.; Iyengar, S. S.; Tomasi, J.; Cossi, M.; Millam, J. M.; Klene, M.; Adamo, C.; Cammi, R.; Ochterski, J. W.; Martin, R. L.; Morokuma, K.; Farkas, O.; Foresman, J. B.; Fox, D. J. *Gaussian 09*, rev. A.02; Gaussian, Inc.: Wallingford, CT, 2016.
(31) Grimme, S. Semiempirical GGA-Type Density Functional Constructed with a Long-Range Dispersion Correction. *J. Comput. Chem.* **2006**, *27*, 1787−1799.
(32) Anderson, B. J.; Guino-O, M. A.; Glueck, D. S.; Golen, J. A.; Dipasquale, A. G.; Liable-Sands, L. M.; Rheingold, A. L. Platinum-Catalyzed Enantioselective Tandem Alkylation/Arylation of Primary Phosphines. Asymmetric Synthesis of p-Stereogenic 1-Phosphaacenaphthenes. *Org. Lett.* **2008**, *10*, 4425−4428.
(33) Tusy, C.; Huang, L.; Jin, J.; Xia, J. Synthesis and Investigation of Novel Thiophene Derivatives Containing Heteroatom Linkers for Solid State Polymerization. *RSC Adv.* **2014**, *4*, 8011−8014.
(34) Lin, I. J.; Nadiv, S. Review of the Phase Transformation and Synthesis of Inorganic Solids Obtained by Mechanical Treatment (Mechanochemical Reactions). *Mater. Sci. Eng.* **1979**, *39*, 193−209.
(35) Bernstein, J.; Davey, R. J.; Henck, J. O. Concomitant Polymorphs. *Angew. Chem., Int. Ed.* **1999**, *38*, 3440−3461.
(36) Jelsch, C.; Soudani, S.; Ben Nasr, C. Likelihood of Atom-Atom Contacts in Crystal Structures of Halogenated Organic Compounds. *IUCrJ* **2015**, *2*, 327−340.

https://dx.doi.org/10.1021/acs.cgd.0c01129
Cryst. Growth Des. 2020, 20, 7460−7469